Supplementary Information:
Local-to-global response of coherent active fluids to localized activity suppression

Opeoluwa J. Balogun,[a] Joshua H. Dickie,[a] Tianhong Xu,[a] Logan Kaelbling,[a] Haoran Wang,[b] and Kun-Ta Wu[a,c,*]

[a] Department of Physics, Worcester Polytechnic Institute, Worcester, Massachusetts 01609, USA
[b] Department of Chemistry and Biochemistry, Worcester Polytechnic Institute, Worcester, Massachusetts 01609, USA
[c] The Martin Fisher School of Physics, Brandeis University, Waltham, Massachusetts 02454, USA
[*]Corresponding: kwu@wpi.edu

Table of Contents

Supplementary Note 1: Response-time analysis of coherent and incoherent active flows

The observed slower relaxation dynamics of coherent active flows compared to incoherent flows following localized activity suppression motivates us to hypothesize that the underlying flow state may influence the timescales over which the active fluid relaxes toward a new steady state (Figs. 1d and 4b). To test this hypothesis, we quantitatively characterize these timescales by analyzing the evolution of the normalized mean flow speed $\langle|\boldsymbol{v}|\rangle/v_0$ following the onset of localized activity suppression and fitting the post-onset $\langle|\boldsymbol{v}|\rangle/v_0$ vs. time data using an exponential relaxation model:

$$\frac{\langle|\boldsymbol{v}|\rangle}{v_0} = V_\infty + (V_i - V_\infty)\, e^{-(t-t_b)/t_r}, \qquad \text{S1}$$

with V_∞, V_i, and t_r as fitting parameters (Supplementary Figure 1a). Here, V_i denotes the initial normalized flow speed prior to the onset while V_∞ denotes the final normalized flow speed after relaxation to the new steady state, and t_r characterizes the exponential relaxation timescale. To capture the time required for the normalized mean flow speed to complete 90% of its total change following the onset, we define the response time $\tau_r \equiv t_r \ln 10$.

To characterize how the response time varies with the dark-arc span θ_b and the underlying flow state, we repeat this analysis across coherent and incoherent experimental datasets for $\theta_b \geq 90°$ (Supplementary Figure 1b), where the flow speed reductions are sufficiently well resolved such that the observed flow-speed changes exceed the intrinsic fluctuations of the flow-speed measurements. Our analysis reveals strikingly different response-time behaviors between incoherent and coherent active flows. For incoherent active flows, the response time remains approximately constant at ~3 minutes across explored dark-arc spans θ_b.[1–3] By contrast, coherent active flows exhibit substantially longer response times reaching 12–14 minutes at intermediate dark-arc spans ($\theta_b \approx 90°$), followed by a gradual decrease with increasing θ_b. Remarkably, when the entire system is darkened ($\theta_b = 360°$), the response time converges to the same ~3-min timescale observed for incoherent active flows.

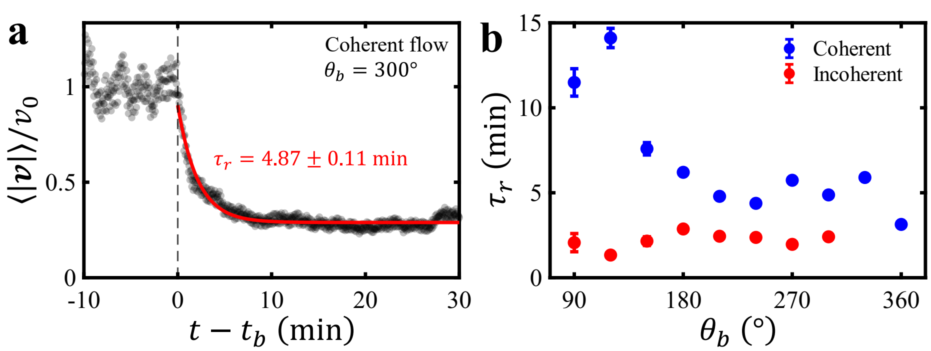

Supplementary Figure 1: Response-time analysis reveals flow-state-dependent relaxation dynamics following localized activity suppression. (a) Representative evolution of the normalized mean flow speed $\langle|\boldsymbol{v}|\rangle/v_0$ for a coherent active flow with $\theta_b = 300°$. Gray dots denote experimental measurements, while the red curve shows the exponential relaxation fit (Eq. S1) with corresponding response time $\tau_r = 4.87 \pm 0.11$ min. The vertical dashed line denotes the onset of localized activity suppression at $t - t_b = 0$. (b) Response time τ_r for coherent (blue) and incoherent (red) active flows across different dark-arc spans θ_b. Error bars denote fitting standard errors.

Supplementary Note 2: Quantification of transition widths across active–dark interfaces

The observations from angular profiles of flow mean speed across active–dark interfaces (Figs. 3a and d and 4d and e) suggest that the flow-speed transitions occur over finite angular widths rather than as abrupt discontinuities. Moreover, these transition widths appear qualitatively similar across explored dark-arc spans (θ_b), interfaces (θ_1 and θ_2), and flow states (coherent and incoherent). To quantify these observations, we systematically analyze the transition widths by fitting the normalized angular flow-speed profiles to a double hyperbolic tangent function:

$$\frac{\langle|\boldsymbol{v}|\rangle_{\mathrm{post}}}{\langle|\boldsymbol{v}|\rangle_{\mathrm{pre}}} = A - \frac{1}{2}(A-B)\left[\tanh\left(\frac{\theta-\theta_1}{l_1}\right) - \tanh\left(\frac{\theta-\theta_2}{l_2}\right)\right], \qquad \text{S2}$$

where $\langle|\boldsymbol{v}|\rangle_{\mathrm{post}}$ denotes the post-onset mean flow speeds while $\langle|\boldsymbol{v}|\rangle_{\mathrm{pre}}$ denotes the pre-onset mean flow speeds; A represents the plateau value outside the dark sector while B represents the plateau values inside the dark sector; θ_1 and θ_2 denote the angular locations of the active–dark interfaces with l_1 and l_2 characterizing the corresponding transition length scales across the interfaces (see dashed vertical lines in Supplementary Figure 2a). Here, angular coordinates are defined relative to the center of the dark sector such that $\theta_1 = -\theta_b/2$ and $\theta_2 = \theta_b/2$. We choose this function as the fitting model because it captures the plateau regions inside and outside the dark sector while allowing independent transition length scales across the two active–dark interfaces. The normalized angular flow-speed profiles are fitted to Eq. S2 with A, B, l_1 and l_2 treated as fitting parameters (Supplementary Figure 2a). The fitted transition length scales l_1 and l_2 are then used to determine the corresponding transition widths $\delta\theta_i \equiv 2.2 l_i$, defined as the angular interval over which the fitted profile changes from 10% to 90% of the plateau difference.

To examine how the transition widths depend on dark-arc spans, interface locations, and flow states, we repeat this analysis across experimental datasets exhibiting well-defined plateau regions inside and outside the dark sector. For coherent-flow experiments, this analysis is performed for θ_b ranging from 90° to 330°, while for incoherent-flow experiments, the analysis is performed for θ_b ranging from 45° to 270°. Outside these ranges, the normalized angular profiles do not exhibit sufficiently stable plateau regions for reliable fitting using Eq. S2. Our analyses for coherent-flow experiments reveal that across the analyzed dark-arc spans, the transition widths remain approximately constant and exhibit no systematic differences between the two active–dark interfaces ($\delta\theta_1$ and $\delta\theta_2$), yielding an average transition width of $\langle\delta\theta\rangle = 22.0 \pm 9.3°$ (Supplementary Figure 2b). Similarly, incoherent-flow experiments exhibit comparable transition widths with an average value of $\langle\delta\theta\rangle = 20.7 \pm 4.3°$ (Supplementary Figure 2c). Together, these results indicate that the finite transition widths are largely independent of dark-arc spans, interface locations, and flow states, suggesting the presence of an intrinsic local length scale governing the transition across active–dark interfaces.

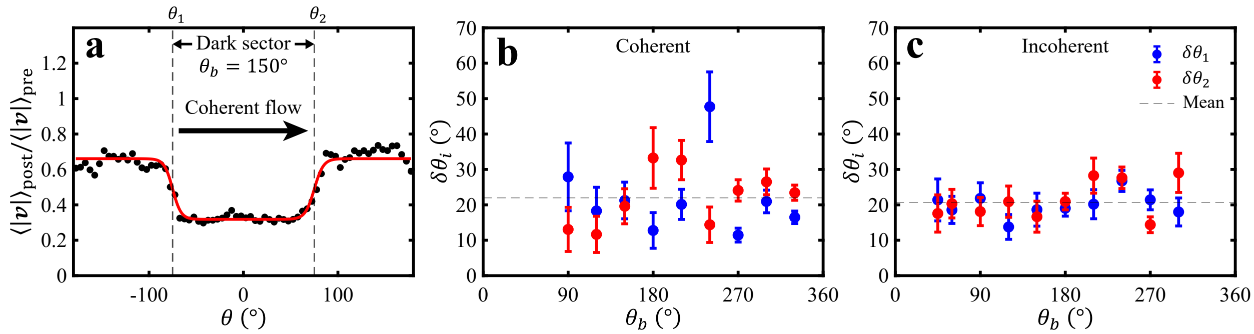

Supplementary Figure 2: Active–dark interface transitions exhibit characteristic widths independent of dark-arc span. (a) Representative angular profile of normalized mean flow speed across the active–dark interfaces for the coherent-flow case with $\theta_b = 150°$. Black dots denote experimental measurements, and the red curve shows the fit using the double hyperbolic tangent model (Eq. S2). Vertical dashed lines denote the dark-sector boundaries located at θ_1 and θ_2. Coherent flow proceeds from negative to positive θ. (b) Transition widths $\delta\theta_i$ across active–dark interfaces for coherent-flow experiments corresponding to the profiles in Fig. 3a and d. Blue dots represent the $\delta\theta_1$ measured at the interface located at θ_1, whereas red dots represent $\delta\theta_2$ measured at θ_2. Error bars denote the fitting standard errors. The dashed horizontal line denotes the mean transition width averaged over all measurements, yielding $\langle\delta\theta\rangle = 22.0 \pm 9.3°$. (c) Same as panel b except for incoherent-flow experiments corresponding to the profiles in Fig. 4d and e. The dashed horizontal line denotes the mean transition width averaged over all measurements, yielding $\langle\delta\theta\rangle = 20.7 \pm 4.3°$.

Supplementary Note 3: Analysis of intrinsic vortex sizes in coherent and incoherent active flows

The observed consistent flow-speed transition widths across active–dark interfaces over a range of dark-arc spans, interface locations, and flow states (Supplementary Figure 2) raise the possibility that the transition widths are governed by an intrinsic characteristic length scale of the active fluid regardless of its flow state. In parallel, we observe that regardless of whether the active fluid is in a coherent or incoherent flow state, the flow streamline structures reveal local vortical structures with similar characteristic sizes despite their distinct global flow state (Figs. 1c and 4a). These observations motivate us to hypothesize that the intrinsic vortex size may be related to the characteristic transition widths across active–dark interfaces.

To test this hypothesis, we analyze all experimental datasets to characterize the intrinsic vortex size of active flows prior to the onset of localized activity suppression. In unconfined active fluids, intrinsic vortex sizes can be characterized using velocity correlation functions.[4–7] However, this approach is not suitable for coherent active flows because long-range coherent circulation dominates the velocity correlations and masks local vortical structures.[8] Therefore, we instead analyze the fluctuations of the vorticity field derived from the in-plane flow velocity field, defined as:

$$\delta\omega(\boldsymbol{r},t) \equiv \omega(\boldsymbol{r},t) - \langle \omega(\boldsymbol{r},t)\rangle_t, \tag{S3}$$

where $\langle \omega(\boldsymbol{r},t)\rangle_t$ denotes the time-averaged vorticity field ($\omega \equiv \partial_x v_y - \partial_y v_x$) prior to the onset of localized activity suppression (Supplementary Figure 3a), followed by analyzing its spatial autocorrelation function defined as:

$$C_{\delta\omega}(\Delta R) \equiv \left\langle \frac{\langle \delta\omega(\boldsymbol{r},t)\ \delta\omega(\boldsymbol{r}+\boldsymbol{\Delta R},t)\rangle_{\boldsymbol{r},t}}{\langle \delta\omega(\boldsymbol{r},t)^2\rangle_{\boldsymbol{r},t}} \right\rangle_{|\boldsymbol{\Delta R}|=\Delta R}, \tag{S4}$$

where $\boldsymbol{\Delta R}$ denotes the spatial displacement vector with magnitude $\Delta R \equiv |\boldsymbol{\Delta R}|$, $\langle\cdot\rangle_{|\boldsymbol{\Delta R}|=\Delta R}$ denotes averaging over displacement vectors with equal separation distance ΔR, and $\langle\cdot\rangle_{\boldsymbol{r},t}$ denotes averaging over spatial positions $\boldsymbol{r}$ and pre-onset times $t - t_b = -10$ to 0 min (Supplementary Figure 3b).

To extract the intrinsic vortex size from the autocorrelation function $C_{\delta\omega}$, we define the first zero-crossing distance $r_{\delta\omega}$ as the characteristic vortex radius (vertical dashed lines in Supplementary Figure 3b). This definition is motivated by the observation that neighboring vortices typically exhibit opposite vorticity, causing the autocorrelation function to decay from positive to negative values across adjacent vortical structures (see red and blue patches in Supplementary Figure 3a). Having defined $r_{\delta\omega}$ as the intrinsic vortex radius, we estimate the intrinsic vortex size as $2r_{\delta\omega}$, corresponding to the approximate vortex diameter. To quantify the characteristic vortex sizes in our active-fluid system, we repeat this analysis across coherent and incoherent experimental datasets prior to the onset of localized activity suppression (Supplementary Figure 3c). Our analysis reveals that the extracted vortex sizes are nearly identical between coherent and incoherent flows, with $2r_{\delta\omega} = 317 \pm 14$ μm for coherent flows and $2r_{\delta\omega} = 320 \pm 8$ μm for incoherent flows. To compare these vortex sizes with the angular transition widths across the active–dark interfaces measured along the toroidal channel, we convert $2r_{\delta\omega}$ into an angular span $\Delta\theta_{\delta\omega} \equiv 2r_{\delta\omega}/r_{\mathrm{mid}}$ using the mid-radius $r_{\mathrm{mid}} \equiv (r_{\mathrm{inner}} + r_{\mathrm{outer}})/2$ of the toroidal channel, yielding $\Delta\theta_{\delta\omega} = 14.7 \pm 0.7°$ for coherent flows and $14.8 \pm 0.4°$ for incoherent flows. These angular vortex spans are on the same scale as the transition widths across active–dark interfaces (Supplementary Figure 2), supporting our hypothesis that the transition widths are related to the intrinsic vortex scale of the active fluid.

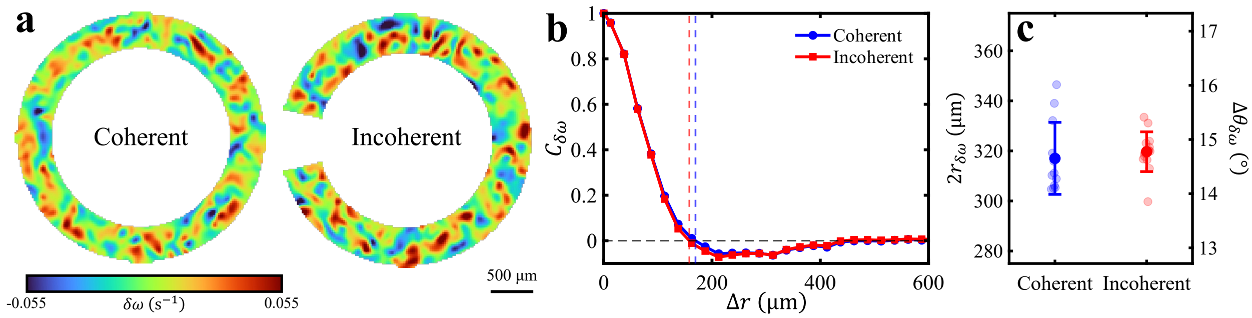

Supplementary Figure 3: Vorticity fluctuation analysis reveals comparable intrinsic vortex scales in coherent and incoherent active flows. (a) Representative colormaps of vorticity fluctuation $\delta\omega$ for coherent (left) and incoherent (right) active flows at $t - t_b = -5$ min prior to the onset of localized activity suppression. Vorticity fluctuations were obtained by subtracting the time-averaged vorticity field from the instantaneous vorticity field to isolate local vortical structures. Red and blue regions denote vortices with opposite vorticity. (b) Spatial autocorrelation functions of vorticity fluctuations $C_{\delta\omega}$ for coherent (blue) and incoherent (red) active flows. Dashed horizontal lines denote zero correlation, while dashed vertical lines indicate the corresponding first zero-crossing distance of $C_{\delta\omega}$ for coherent (blue) and incoherent (red) active flows. (c) Characteristic vortex sizes $2r_{\delta\omega}$ extracted from the first zero-crossing distances of $C_{\delta\omega}$ for coherent (blue) and incoherent (red) active flows. Faint dots denote individual measurements, while solid dots and error bars denote the mean and standard deviation across datasets. The right axis shows the corresponding angular spans $\Delta\theta_{\delta\omega}$ of the vortex.

Supplementary Movie 1: Experimental evolution of coherent active-fluid flows following localized activity suppression. Time-lapse fluorescence microscopy of passive fluorescent tracer particles suspended within microtubule–kinesin active fluids confined within toroidal channels under patterned illumination with dark-arc spans $\theta_b = 30°$ (left), $90°$ (middle), and $360°$ (right). The movies are aligned relative to the onset time of localized activity suppression (t_b). Red dashed boundaries appearing after $t - t_b = 0$ denote the dark sectors. Coherent circulation persists despite localized activity suppression. Notably, this persistence extends to the condition where the dark sector encompasses the entire system ($\theta_b = 360°$, right), because the projector-generated dark region retains a small residual blue-light intensity rather than complete absence of illumination (see Methods).

Supplementary Movie 2: Experimental evolution of incoherent active-fluid flows following localized activity suppression. Time-lapse fluorescence microscopy of passive fluorescent tracer particles suspended within microtubule–kinesin active fluids confined within broken toroidal channels under patterned illumination with dark-arc spans $\theta_b = 30°$ (left), $90°$ (middle), and $300°$ (right). The movies are aligned relative to the onset time of localized activity suppression (t_b). Red dashed boundaries appearing after $t - t_b = 0$ denote the dark sectors. In contrast to coherent-flow experiments (Supplementary Movie 1), the response to localized activity suppression remains primarily localized within the dark sectors.

Supplementary Movie 3: Simulated evolution of active-fluid flows following localized activity suppression. Evolution of midplane ($z = 0$) streamlines of the in-plane velocity field overlaid on the corresponding in-plane flow speed magnitude $\sqrt{v_x^2 + v_y^2}$ for coherent flow with motor transport (top), coherent flow without motor transport (middle), and incoherent flow with motor transport (bottom). Localized activity suppression with $w/L = 0.12$ is introduced at $t = t_b = 310$. Vertical dashed lines appearing after $t = t_b$ denote the dark-sector boundaries. Both coherent-flow cases (with/without motor transport) remain globally ordered after the onset of localized activity suppression, whereas the incoherent-flow case remains vortex-dominated.

Supplementary Movie 4: Experimental evolution of active-fluid flows before and after coherent-flow formation under sequential illumination. Time-lapse fluorescence microscopy of passive fluorescent tracer particles suspended within microtubule–kinesin active fluid confined within a toroidal channel. A dark arc ($\theta_b = 90°$) is imposed immediately upon activation (Phase I) for 30 minutes, followed by uniform ring illumination (Phase II) for 20 minutes, after which the same dark arc is reintroduced (Phase III). Red dashed boundaries denote the dark sector when present. The same dark arc produces markedly different flow responses when applied before and after coherent circulation is established.

Supplementary References

1. Zarei, Z., Berezney, J., Hensley, A., Lemma, L., Senbil, N., Dogic, Z. & Fraden, S. Light-activated microtubule-based two-dimensional active nematic. *Soft Matter* **19**, 6691–6699 (2023).
2. Nishiyama, K., Berezney, J., Norton, M. M., Aggarwal, A., Ghosh, S., Zarei, Z., Hagan, M. F., Fraden, S. & Dogic, Z. Closed-loop control of active nematic flows. *Physical Review X* **15**, 041053 (2025).
3. Vélez-Cerón, I., Ignés-Mullol, J. & Sagués, F. Active nematic coherence probed under spatial patterns of distributed activity. *Soft Matter* **20**, 9578–9585 (2024).
4. Fan, Y., Wu, K.-T., Aghvami, S. A., Fraden, S. & Breuer, K. S. Effects of confinement on the dynamics and correlation scales in kinesin-microtubule active fluids. *Physical Review E* **104**, 034601 (2021).
5. Bate, T. E., Varney, M. E., Taylor, E. H., Dickie, J. H., Chueh, C.-C., Norton, M. M. & Wu, K.-T. Self-mixing in microtubule-kinesin active fluid from nonuniform to uniform distribution of activity. *Nature Communications* **13**, 6573 (2022).
6. Henkin, G., DeCamp, S. J., Chen, D. T. N., Sanchez, T. & Dogic, Z. Tunable dynamics of microtubule-based active isotropic gels. *Philosophical Transactions of the Royal Society A: Mathematical, Physical and Engineering Sciences* **372**, 20140142 (2014).
7. Sanchez, T., Chen, D. T. N., DeCamp, S. J., Heymann, M. & Dogic, Z. Spontaneous motion in hierarchically assembled active matter. *Nature* **491**, 431–434 (2012).
8. Wu, K.-T., Hishamunda, J. B., Chen, D. T. N., DeCamp, S. J., Chang, Y.-W., Fernández-Nieves, A., Fraden, S. & Dogic, Z. Transition from turbulent to coherent flows in confined three-dimensional active fluids. *Science* **355**, eaal1979 (2017).